Journal of Materials Chemistry A

Light-Ferroelectric Interaction in Two-Dimensional Lead Iodide Perovskites

Journal:	*Journal of Materials Chemistry A*
Manuscript ID	TA-ART-12-2021-010944.R1
Article Type:	Paper
Date Submitted by the Author:	08-Mar-2022
Complete List of Authors:	Kim, Dohyung; University of Tennessee Knoxville College of Engineering Ievlev, Anton; Oak Ridge National Laboratory, Center for Nanophase Materials Sciences Ovchinnikova, Olga; Oak Ridge National Laboratory, Computational Science and Engineering Division Kalinin, Sergei; Oak Ridge National Laboratory, Center for Nanophase Materials Sciences Ahmadi, Mahshid; University of Tennessee, Materials Science and Engineering

Light-Ferroelectric Interaction in Two-Dimensional Lead Iodide Perovskites

Dohyung Kim[1], Anton V. Ievlev[2], Olga S. Ovchinnikova[3], Sergei V. Kalinin[2], Mahshid Ahmadi[1*]

[1]*Institute for Advanced Materials and Manufacturing, Department of Materials Science and Engineering, University of Tennessee, Knoxville, TN 37996, USA*

[2]*Center for Nanophase Materials Sciences, Oak Ridge National Laboratory, Oak Ridge, TN 37830, United States, USA*

[3]*Computational Science and Engineering Division, Oak Ridge National Laboratory, Oak Ridge, TN 37830, United States, USA*

*Corresponding authors' email: mahmadi3@utk.edu

Abstract

The unique physical properties of two-dimensional (2D) metal halide perovskites (MHPs) such as nonlinear optics, anisotropic charge transport, and ferroelectricity have made these materials promising candidates for multifunctional applications. Recently, fluorine derivatives such as 4,4-difluoropiperidinium lead iodide perovskite or (4,4-DFPD, $C_5H_{10}F_2N)_2PbI_4$ has shown strong ferroelectricity as compared to other 2D MHPs. Although it was previously addressed that the ferroelectricity in MHPs can be affected by illumination, the underlying physical mechanisms of light-ferroelectricity interaction in 2D MHPs are still lacking. Here, we explore the electromechanical responses in 4,4-$(DFPD)_2PbI_4$ thin films using advanced scanning probe microscopy techniques revealing ferroelectric domain structures. Hysteretic ferroelectric loops measured by contact-Kelvin probe forcemicroscopy are dependent on domain structures in dark condition, while ferroelectricity weakens under illumination. X-ray diffraction patterns exhibit significant change in preferential orientation of individual lattice planes under illumination. Particularly, the reduced intensity of the (1 1 1) lattice plane under illumination leads to transitioning from a ferroelectric to paraelectric phase. The instability of positive ions, especially molecular organic cations is observed under illumination by time-of-flight secondary ion mass spectrometry. The combination of crystallographic orientation and

chemical changes under illumination clearly contribute to the origin of light-ferroelectricity interaction in 2D (4,4-DFPD, $C_5H_{10}F_2N)_2PbI_4$.

Keywords: light-ferroelectricity interaction, two-dimensional ferroelectric, metal halide perovskites, cKPFM, hysteretic behavior.

Introduction

Metal halide perovskites (MHPs) have gained much attention from the scientific community due to their easy and inexpensive fabrication method, and their outstanding optoelectronic properties.[1-3] As compared to the three-dimensional (3D) structure, 2D layered MHPs have a greater structural diversity due to breaking the tolerance space of the 3D framework.[4] 2D MHPs have shown higher ambient stability resulting from a strong interlocking force between the organic and inorganic species.[5] In addition, these class of perovskites have shown unique physical characteristics such as optical nonlinearity[6], anisotropic charge carrier transport[7], large exciton binding energy[8], and ferroelectricity[9]. Thus, 2D MHPs can be promising candidates in many optoelectronic functionalities.

Typically, ferroelectricity i.e. the switchable polarization with long-range ordered domains and hysteretic behavior is suitable for applications in nonlinear optical applications, nonvolatile memory, and energy storage devices.[10] Recently, ferroelectricity has been frequently observed in a number of 2D MHPs[11-19]. The 2D MHP ferroelectrics have a general chemical formula of A_2BX_4 where large organic cations are placed between the inorganic layers (BX_4)[9]. This structure allows 2D MHPs to have multiple quantum wells, in addition to the large freedom of organic cation motions which lead to ferroelectricity in these materials.

The one effective strategy for higher spontaneous polarization (P_s) in 2D MHP ferroelectrics is to design the A-site cations by substitution of hydrogen with fluorine.[20, 21] The fluorine substitution as the most electronegative element, with a van der Waal's radius of around 147 pm which is similar to that of hydrogen atom (120 pm) can have a minor structural distortion for tuning the physical properties, e.g., polarization state. This can be found in recently developed 2D MHPs showing stronger ferroelectricity.[22, 23] Most recently, 4,4-difluoropiperidinium (DFPD) that includes fluorine derivatives was introduced into PbI_4 octahedral layers, resulting in higher P_s ~10 $\mu C/cm^2$ at room temperature[17]. This 2D composition possesses relatively larger spontaneous polarization as compared to other molecular ferroelectrics[9]. Our recent study demonstrated that ferroelectricity can be only observed in the low strain $(4,4\text{-DFPD})_2PbI_4$ thin films.[24] Nevertheless, further efforts to elucidate underlying mechanisms behind ferroelectricity are necessary for this material.

Particularly, the interplay of light and ferroelectricity, the so-called photo-ferroelectricity, is an important scientific question as ferroelectricity in MHPs remains an

academic curiosity. The light-ferroelectricity interaction including bulk and depolarization field-driven photovoltaic effects, domain wall motions, and Schottky barrier effect, has been extensively studied in classical ferroelectrics and 3D MHPs.[25] Despite numerous efforts, the interplay of light and ferroelectricity is unexplored in 2D MHPs. It is well known that the ferroelectricity in 2D MHPs stems from the dipole moment of organic cations. Ferroelectricity has been experimentally demonstrated using various characterization tools. However, the potential possibilities such as chemical dynamics and crystallographic orientations, directly correlating with ferroelectricity have not been studied yet. In fact, the interplay between surface-charged ions and bulk spontaneous polarization can lead to mixed states in ferroelectric films.[26] Unlike classical ferroelectrics, highly ordered ionic states in MHPs provide an electrochemically driven polarization, which has led to ferroelectric-like behaviors in 3D polycrystalline perovskite films.[27] Even though the mobile ions in 2D MHPs are tightly locked as compared to 3D counterparts, ion migration still exists in 2D MHPs[28], thus it is essential to explore the origin of ferroelectricity in materials with ion dynamics. Another important implication is crystallographic orientation. It has been well established that crystallographic orientations in MHPs have an impact on optoelectronic properties such as surface photovoltage, charge transport, and charge carrier recombination.[29-31] Our recent studies discuss the correlation between crystallographic orientations and ferroelastic twin domains in 3D MHPs.[32] This study reveals that different crystallographic orientations between adjacent twin domains contribute to non-ferroelectricity.[32] The intrinsic properties of 2D MHPs could possibly change under illumination leading to interesting phenomena[33-35] as observed in 3D MHPs. These have motivated us to explore the light interaction with ferroelectricity in 2D $(4,4\text{-DFPD})_2PbI_4$.

In this study, $(4,4\text{-DFPD})_2PbI_4$ crystals are successfully grown by a slow cooling crystallization method and then thin films are fabricated by drop-casting from the as-grown crystals dissolved in dimethyl sulfoxide. Details of crystal growth and film fabrication can be found in our previous work[24]. We explore the electromechanical responses on the film surface using band excitation piezo-response force microscopy (BE-PFM). Further, contact Kelvin probe force microscopy (cKPFM) an advanced piezo-response force microscopy (PFM), detects the electromechanical responses using a first-order reversal curve (FORC) electrical waveform that is composed of gradually increasing and decreasing stepwise electrical biases. To investigate the light effect, we perform cKPFM measurements under illumination after the measurement in dark. X-ray diffraction (XRD) is carried out to study crystallographic orientations under external stimuli such as illumination and electric bias. Time-of-flight

secondary ion mass spectrometry (ToF-SIMS) is performed to demonstrate the chemical dynamics of the film surface in dark and under light conditions. Our results elucidate the origin of the light-ferroelectricity interaction in (4,4-DFPD)$_2$PbI$_4$ thin films.

Results & Discussions

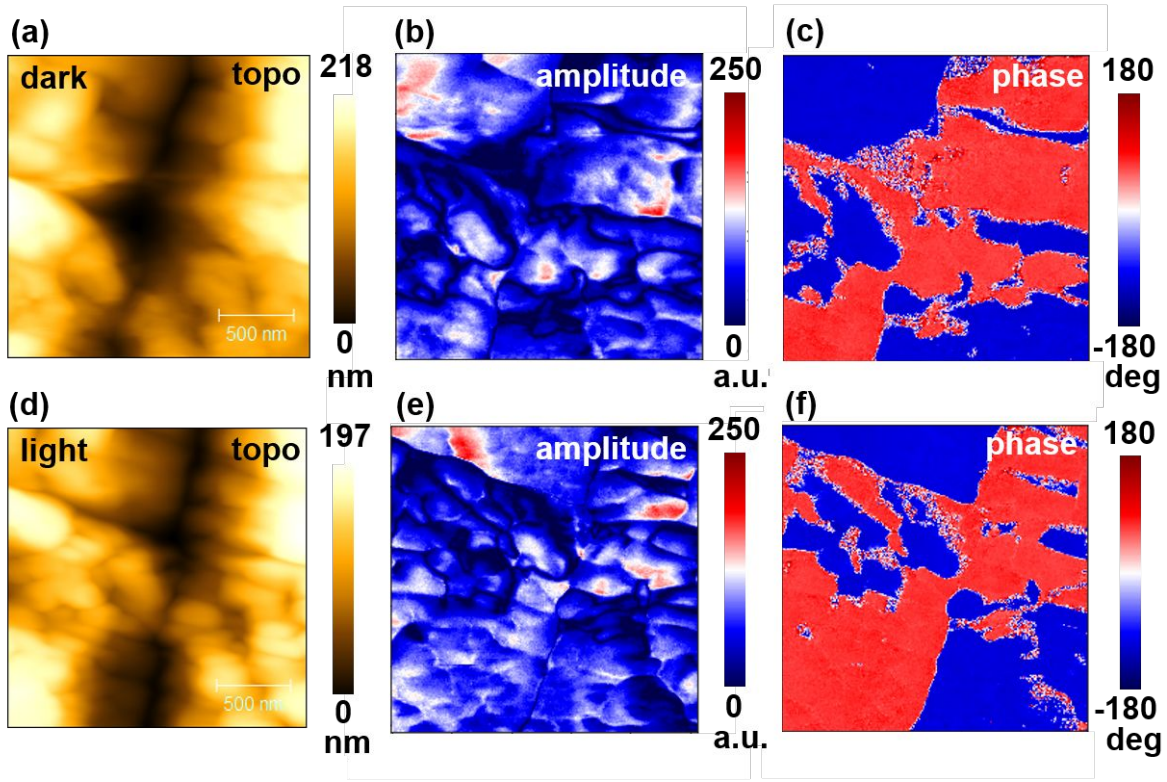

Figure 1. BE-PFM images of the $(4,4\text{-DFPD})_2PbI_4$ thin film in dark (top row) and under illumination (bottom row). The full scan size is over an area of $2\mu m^2$. (a) Topography, (b) BE-PFM amplitude, and (c) phase in dark and (d-f) under illumination.

Our previous study demonstrated that only $(4,4\text{-DFPD})_2PbI_4$ thin films fabricated by drop-casting leads to superior ferroelectricity.[24] To investigate the electromechanical responses and ferroelectricity on the film surface, the scanning probe microscopy (SPM) including atomic force microscopy (AFM), PFM, BE-PFM, and cKPFM measurements were performed in dark and under illumination using Asylum Research AFM (MFP-3D) with a Labview/National Instruments setup. BE measurements e.g., BE-PFM and cKPFM were carried out by tracking the contact resonance frequency in BE mode. Note that all measurements were taken under ambient air in a low relative humidity below 20%. We note that the samples were stable and did not show any topological changes during repetitive scans in the same areas.

Figure 1 shows the corresponding topography, BE-PFM amplitude, and phase in $(4,4\text{-DFPD})_2PbI_4$ thin film in dark and under illumination. Other BE-PFM frequency and quality factor (Q) maps are displayed in Figure S1. The selected scan areas in Figure 1 are chosen from the larger scans (see Figure S2), revealing ferroelectric domains in the phase maps. In dark, the observed electromechanical amplitude responses (Figure 1b) are almost similar as compared

to the responses under illumination (Figure 1e). To compare the amplitude responses between two conditions, histogram plots are shown in Figure S3 and additional explanation including the results of a standard ferroelectric sample is described in Supplementary Note 1. As previously shown by us[24], ferroelectric domains are revealed by the phase flips of 180° in both phase maps (Figure 1c, f). However, academic curiosity still remains regarding the observed ferroelectric domains' properties and their origin in 2D MHPs which can be further studied. Nonetheless, the alternating domain structures are clearly visible in similar locations both in dark and under illumination. Note that the ferroelectric domains in $(4,4\text{-DFPD})_2PbI_4$ thin film was confirmed via BE-PFM by us[24] and classical PFM by others[17].

PFM techniques have limited insight into electromechanical responses especially when the film surfaces are not smooth since the larger topological changes generally can lead to measurement artifacts. Thus, we utilize the cKPFM technique as an advanced PFM mode, exploring both electromechanical and electrostatic phenomena using complex electrical pulsed bias waveform.[36, 37] In cKPFM spectroscopy, gradual stepwise pulsed biases with on- and off-field, the so-called first order reversal curve (FORC) (see Figure 2a), applies to a conductive AFM tip where the biases are denoted as V_{write} and V_{read}. The V_{write} (DC pulse) is used to change the functional response, e.g., surface potential or ferroelectric switching while the V_{read} as a subsequent small DC voltage track changes in electrostatic forces.

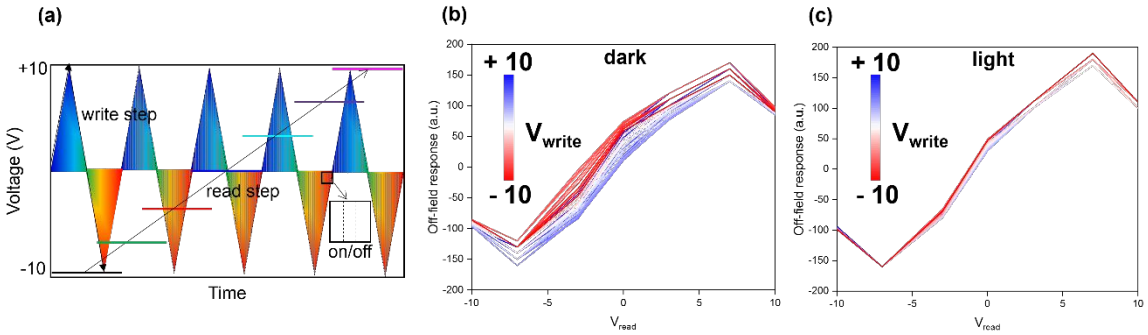

Figure 2. (a) Schematic illustration of FORC electrical bias waveform in cKPFM measurements. Averaged cKPFM curves on a 40 × 40 grid with a 2 × 2 μm area upon application of different pulsed bias voltage (b) in dark and (c) under illumination.

As discussed, we perform cKPFM measurements in similar regions in dark and under illumination. Figure 2 shows averaged cKPFM responses from all 1600 pixels over an area of 2 μm^2 as a function of biases, ranging from -10V to +10V. Here, the duration of the bias steps is around 16 milliseconds (ms). The choice of 16 ms time step is limited by the bandwidth of the cKPFM measurement. This method utilizes a complex waveform comprised of multiple hysteresis loops per each spatial pixel. Given the limitation of 1-10 s per spatial pixel, the duration of the single-bias step cannot exceed 10-20 ms. At the same time, given the relatively weak PFM signal in this material where cKPFM responses are basically from the multiplication of PFM amplitude and phase responses, smaller bias times result in unacceptably low signal-to-noise ratios. The used millisecond pulse duration in cKPFM measurements allows exploring ferroelectricity. Specifically, this time scale with on- and off-fields leads to injection and relaxation of charge carriers, and then polarized charge states (ferroelectric responses) are measured during off-field conditions. The millisecond time scale in dark condition could activate electronic charge carriers in MHPs and charge injection, rather than ion migration that occurs within either sub- or several seconds or minute time scale as demonstrated in many studies[38-43]. However, at high biases the applied pulse duration could also drive ion migration. Therefore, during our measurements, it is expected that both electronic and ionic charge carriers transit in 2D MHPs. However, this phenomenon is less effective than in 3D MHPs due to suppressed ionic motions in 2D MHPs[44] in that there is a strong interlocking force between organic and inorganic sublattice. Note that the spectroscopic experiments were performed consecutively from top-left to right, move to the next line, and then down to the 40th line in the same way in dark and then under illumination. During the measurements under illumination, the scanned location was slightly shifted (a few micrometers) due to thermal drift as the

measurements take over 17 hours but both locations in dark and under illumination are within one large crystal (Figure S2c). Besides, we cannot observe any topological change after both measurements. Thus, we believe that our results are not directly correlated with the damaged film surface. Nonetheless, we cannot completely rule out the internal changes by photogenerated charge carriers in the bulk films during the measurements. To verify if this phenomenon is due to accumulated bias steps, we perform two consecutive cKPFM measurements on the same location in dark. Despite slightly different responses, similar results are revealed in Figure S4. Thus, it is apparent that the cKPFM response with narrow bands in Figure 2c results from illuminating the film surface.

As described above, it is interesting to note that the band dispersions in cKPFM curves are significantly different between dark and light conditions in Figure 2b-c. We previously observed hysteretic responses at some specific locations in the same material[24], which were also offset by many non-hysteretic responses. Consequently, in the averaged cKPFM responses, hysteretic behaviors can be significantly reduced. Similarly, in the current study, the hysteretic behaviors are significantly decreased in both conditions due to either less hysteretic or non-hysteretic responses at more pixels. Particularly, while larger band dispersion is observed in dark, the cKPFM response is narrow and almost linear under illumination. In Figure2b-c, cKPFM data is from the averaged curves of all pixels. As a result, band dispersion depends on the number of data points with lower band dispersion. According to our previous studies[45, 46], larger band dispersion is induced under illumination in 3D MHPs due to the higher density of charge carriers. In fact, the linear curve in cKPFM responses is associated with pure electrostatic behavior and transition to paraelectricity while the larger band dispersion is induced by higher density of charge carriers including photogenerated charge carriers and mobile ion species. Nonetheless, our results reveal the larger band dispersion only in dark as compared to light condition. Therefore, we further investigate cKPFM curves in individual pixels comparing ferroelectric domain structures in the next section.

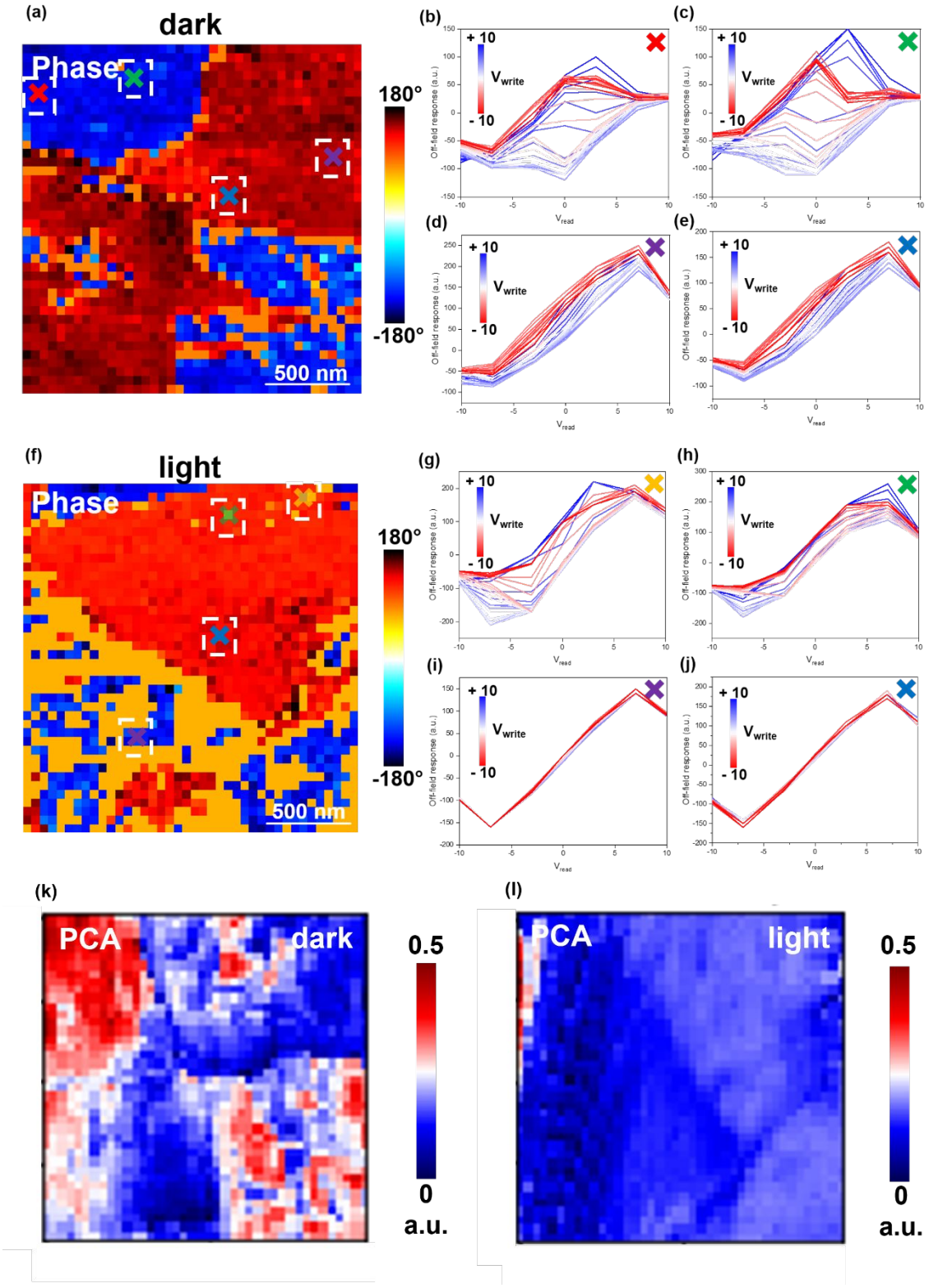

Figure 3. (a) The loading map of phase responses in cKPFM measurements in dark where the ferroelectric domain is observed in BE-PFM measurements. Individual cKPFM curves at the '×' marked in (b) red, (c) green, (d) purple, and (e) light-blue in (a). (f) The loading map of phase responses in cKPFM measurements under illumination. Individual cKPFM curves at the '×' marked in (g) yellow, (h) green, (i) purple, and (j) light-blue in (f). The 1st PCA component of mean deviation from cKPFM data (k) in dark and (l) under illumination.

Figure 3a-j shows the corresponding loading map of phase responses and cKPFM curves in several representative pixels in dark and under illumination. In dark, the phase map in Figure 3a shows the corresponding domain structures as shown in Figure 1. Other responses including amplitude, frequency, and Q-factor maps are displayed in Figure S5. We rule out the areas marked in red circles in Figure S5b as a significant shift of contact resonance leads to artifacts in the responses. This frequency shift originates from larger topographic variations. Interestingly, we observe strong hysteretic behaviors (Figure 3b-c) at blue regions in the phase maps while less hysteretic behaviors (Figure 3d-e) are observed in red regions of the phase maps. To further investigate hysteretic behaviors at more pixels, we have shown more cKPFM responses in Figure S6-7. As a result, the larger hysteresis loops in the cKPFM responses correspond to the blue regions in the phase map while the reduced hysteresis loops are observed at the red regions in the map. Our results indicate that local hysteretic dynamics are dependent on either orientation of polarization or domain structure. Such switchable electromechanical responses stem from various parameters such as charge injection, ion migration, and the electrochemical strain by ionic motions.[47] We will discuss the chemical dynamics studied by ToF-SIMS in this material in the later section.

To explore the potential role of ion dynamics, we apply FORC biases to the film surface through the AFM tip which results in hysteretic behaviors in cKPFM curves. Note that it requires a higher electric field (>30V) for complete domain switching as described by Xiong et al.[17] However, it has been previously demonstrated via cKPFM that the FORC bias can allow lower switching biases (<10V) in cKPFM curves, compared with normal on-field bias sweep. This is due to either different film quality or accumulated bias steps during FORC biases. It is well known that the non-ferroelectric effects can also lead to hysteresis in PFM that convincingly imitates the ferroelectric behaviors with bistable states.[47] Thus, clarifying the ferroelectricity at the nanoscale is not confined to only PFM study. With this demand, it has been well established that cKFPM is a complementary technique allowing to distinguish between ferroelectric and non-ferroelectric materials.[37] Therefore, we adopt the cKPFM technique to identify the ferroelectricity and ionic motions in 2D MHPs. Despite the ongoing controversy in 3D MHPs, the ferroelectricity is consistently observed in 2D MHPs via various characterization tools such as PFM[11, 12, 14-19, 24], current-voltage (*I-V*) characteristic[11, 12, 15, 17-19], polarization-electric (P-E) loop[11-13, 15-19], permittivity[11-15, 17, 19], second harmonic generation (SHG)[11-15, 17-19], and cKPFM[24].

Here, despite an effective ferroelectric behavior in dark, the observed ferroelectricity is significantly reduced under illumination as shown in Figure 3f-j. Particularly, the minor hysteretic behaviors (see Figure 3g-h) are only observed at a few pixels. The noticeable lower band dispersion under illumination in Figure 3i-j, indicates the non-ferroelectric nature of the film. In cKPFM response, the band dispersion is a measure of the charge injection onto the film surface where larger band dispersion represents a higher density of charge carriers.[48, 49] As shown in cKPFM response under illumination, the narrow band dispersion (Figure 3i-j) identifies the pure electrostatic nature as non-ferroelectricity. Further, the linear shape (lower band dispersion) in cKPFM response results from transition to paraelectricity.[50] Other responses including amplitude, frequency, and Q-factor maps are displayed in Figure S8. Additional cKPFM curves at different pixels are shown in Figure S9-10. However, most of pixels exhibit linear cKPFM curves indicating either weak or no ferroelectricity regardless of domain structures under illumination.

In our cKPFM results, band dispersion is strongly dependent on the negative and positive PFM phases in dark condition, which corresponds to the opposite orientation of spontaneous polarization in different ferroelectric domains. We suspect that such dependence in dark conditions derives from chemical inhomogeneity or differences in local crystallographic orientations. These properties can contribute to localized ferroelectric or non-ferroelectric nature in 2D MHPs. Under illumination, such dependence disappears due to the absence of ferroelectric behavior. This local polarization is frequently observed in classical oxides[51] and originates from the inhomogeneity of surface defects. Thus, the observed local ferroelectricity can be due to several reasons such as chemical inhomogeneity, variation in preferential crystallographic orientation, presence of defects, and their redistribution.

To further analyze the cKPFM data and separate the noise signals from the complex coupled responses in original data, principal component analysis (PCA) from the mean deviation of cKPFM data is performed on both spectroscopy maps in dark and under illumination. We choose the PCA approach as this is one of the classical dimensionality reduction techniques with a relatively low computational cost for large dataset. Our recent study provides a detail explanation of PCA approach in cKPFM data.[45] From the PCA analysis, the 4D cKPFM data (V_{read}, V_{write},x, y) can be deconvoluted to 3D data set R_{av} (V_{read}, x, y) where R_{av} represents the average responses. The cKPFM data set is analyzed by PCA as below:

$$PCA\ Space\ (R^k) = \sum_{i=1}^{N} R^M(x_i - \mu)$$

Where R^M, x_i, and μ represent original space, centering data, and mean. To preserve the original data, we have selected the most k eigenvectors, e.g. $\{V_1, \ldots, V_k\}$ in PCA space. Here, the number of the optimized components (eigenvectors) is three. Figure 3k-l shows the loading maps of the 1st PCA component in dark and under illumination. The loading maps show spatial distribution of the averaged responses in cKPFM data set. The eigenvectors (R_{av}) for the 1st component as a function of V_{read} are presented in Figure S11. There are the same trends for R_{av} in both conditions, which is related to pure electrostatic response. The 2nd and 3rd components are displayed in Figure S12. The loading map in the 2nd component (Figure S12a) also shows red color regions with a downward trend of R_{av} response. However, there are noise responses in the 3rd component since R_{av} is not straightforward. As the 3rd component is not meaningful due to noise response, thus we only consider the 1st and 2nd components that are related to pure electrostatic response from the PCA approach. Nonetheless, the red color regions in the 1st component (Figure 3k) are well matched with hysteretic behaviors as analyzed in the original data. The red color regions are remarkably clustered in the dark while these regions can be seen rarely under illumination (Figure 3l). These non-contrast responses are the same in the 2nd component (see Figure S12c). This phenomenon is unique as typically light drives the enhanced ferroelectric polarization in classical ferroelectrics[52, 53]. Hence it is necessary to further study the origin of the light-ferroelectricity interactions in this material.

It is known that in MHPs, the photogenerated charge carriers under illumination can contribute to the higher density of charge carriers. Thus, such smaller band dispersion can be associated with the absence of ferroelectricity under illumination rather than simply reduced density of charge carriers. The weakened ferroelectricity can be possibly due to a change of preferential crystallographic directions and organic cation decomposition which is explored in the following section. Another possible scenario is that if higher band dispersion in cKPFM response originates from the interplay between injected charge carriers and intrinsic defects, e.g., trapped/detrapped charge carriers, in dark conditions, excess photogenerated charge carriers can fill the traps, which leads to reduction of band dispersion due to decrease of defect densities. This will be explored in our future studies. However, as shown the ferroelectricity is

reveled in this 2D MHPs, thus lowering band dispersion is significantly responsible for weak ferroelectricity response under illumination.

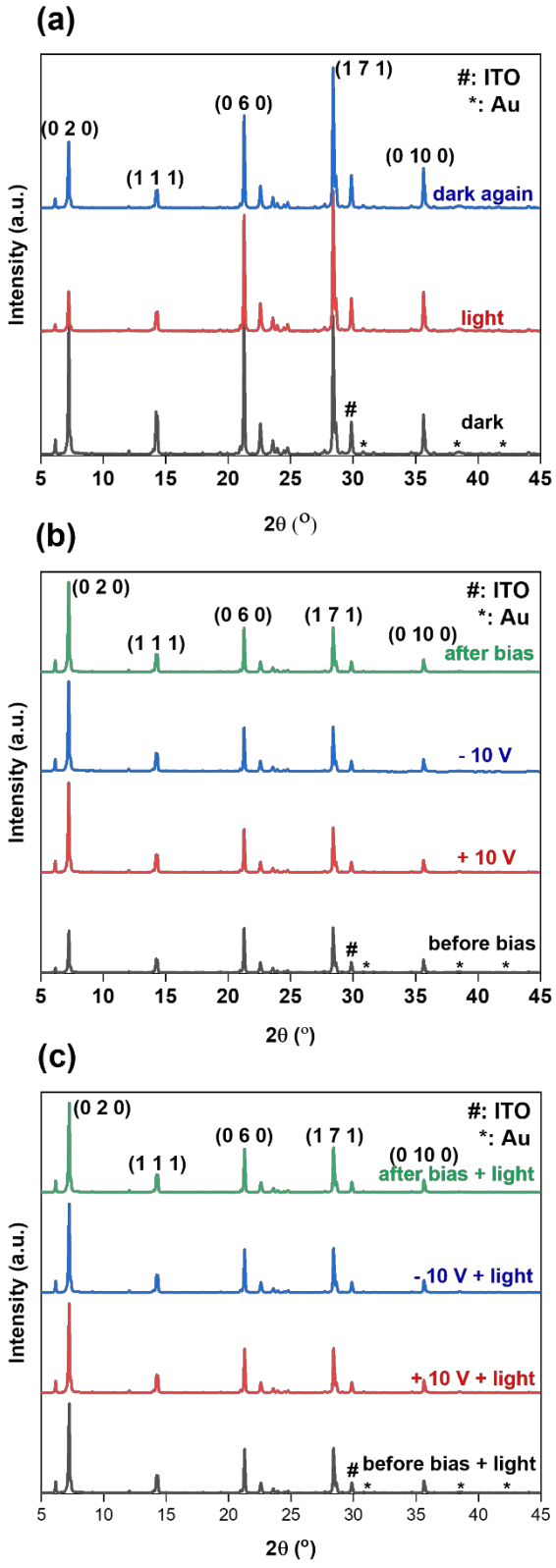

Figure 4. The in-situ XRD measurements. (a) The overlaid XRD patterns in dark-illumination-dark conditions, (b) before and after biasing with +10 V, and –10 V, and back to no bias in dark, (c) before and after biasing with +10 V and –10 V under illumination and back to the pristine (no bias, dark condition).

To explore the origin of light-ferroelectricity interaction, we perform in-situ XRD measurements under illumination and upon application of electric bias. The biases are applied vertically to a planar device structure to provide similar experimental conditions to the cKPFM measurements, which is described in Figure S13. For this measurement, we deposited a thin layer of Au electrode (around 50 nm) on top of the perovskite film surface. Note that source bias is connected to the bottom ITO electrode. During our measurements, there is no major damage to the film structure by showing new diffraction peaks such as PbI_2 near 15° as evidence for degradation of the film[54]. Besides, we cannot find any remarkable changes in the peaks related to Au and ITO as marked with star and hash, respectively.

Figures 4a-c show the overlaid XRD patterns of light and bias conditions. The extent of crystallinity on individual planes is variable depending on the electrical bias as well as under illumination. Firstly, it is evident that some planes, especially the peaks below 25° are influenced by illumination as shown in Figure 4a. The enlarged XRD peaks in Figure 4a are presented in Figure S14. Particularly, as shown in Figure S14a, the peak intensity of (0 2 0) plane decreases under illumination and then it is partially back to the pristine condition when the sample is back to dark. However, the intensity of (1 1 1) plane (Figure S14b) does not return to the original condition after the intensity decreases by illumination. In addition, the intensity of (0 6 0) plane (Figure S14c) under illumination is further decreased when the sample is back to the dark condition. We note that the rest of the planes beyond 25° 2θ, do not change during the experiment (Figure S14d). The changes in the XRD peak intensities can be associated with structural changes. Our previous study demonstrated light-induced structural variations measured by peak broadening from in-situ XRD measurements in 3D MHPs.[35] However, we cannot observe the pronounced peak broadening in the XRD results of 2D MHPs due to a more stable structure, which could be attributed to the variation in the degree of crystallinity. It should be noted that the light intensity may change the structure. Here, we use an LED light source with an intensity of ~ 5 mW/cm^2. Next, we explore the effect of electrical bias on crystallinity of 2D perovskite sample. Figure 4b shows the overlaid XRD patterns when a positive and negative biases ±10 V is applied to the sample in dark. Interestingly, significant increase in the intensities of XRD peaks are observed in particular the (0 2 0), (1 1 1), and (0 6 0) plans once +10 V is applied to the device (see Figure S15a-c). The increased intensity remains constant during the application of –10 V. Despite the removal of biases, the change in the intensities of peaks is not reversible. Similarly, the rest of the peaks beyond 25° 2θ (Figure S15d) remains constant during our measurements. Then, we perform XRD measurements by

applying electrical biases under illumination as shown in Figure 4c. However, we do not observe any noticeable changes in the XRD peaks. Continuous application of bias results in an irreversible effect on the crystallinity (see Figure 4c). Note that electric field in this measurement is much stronger as compared to the application of FORC bias (on- and off-fields with 16 millisecond duration) for the cKPFM measurements. Nonetheless, from our XRD studies, it is observed that the (0 2 0), (1 1 1), (0 6 0) lattice planes are more sensitive to the light-induced crystallinity change. For the 2D perovskite crystals, a crystallographic direction along [001] is associated with the ferroelectric phase due to perpendicular polarization direction between quantum wells while the [110] directions lead to the paraelectric phase.[17] Hence, growth of (0 2 0) plane can annihilate the ferroelectric behavior rather than that of (1 1 1) plane in our result (Figure 4a). This crystallographic orientation-modulated ferroelectricity is previously observed in classical ferroelectrics.[55-57] It can be argued that the significant growth of horizontal plane induced by illumination and electrical biases contributes to the removal of ferroelectricity in this material.

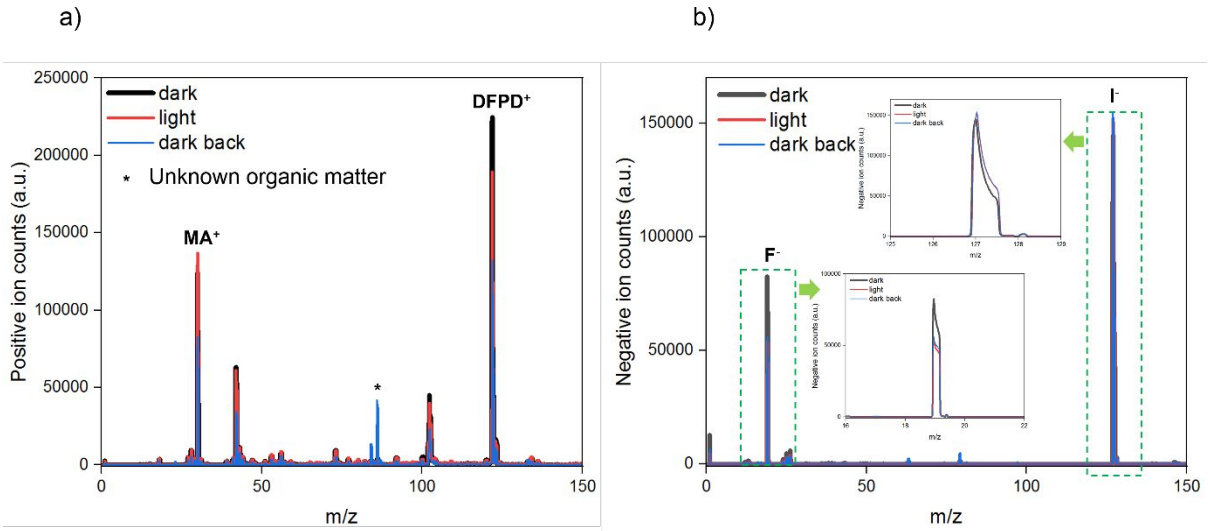

Figure 5. Time of Flight Secondary Ion Mass Spectrometry (ToF-SIMS) of (a) positive ions and (b) negative ions in dark-illumination-dark conditions. The mainly contributed components represent $DFPD^+$ and MA^+ ions in the mass spectra of positive ion and the major peaks are I^- and F^- in the mass spectra of negative ion.

To further elucidate the origin of light-ferroelectricity interaction, we perform ToF-SIMS on 2D perovskite film in dark and under illumination. The mass spectra of positive and negative ions are shown in Figure 5. As can be seen in the spectra of positive ions (Figure 5a), the $DFPD^+$ ion concentration distinctly decreases under illumination as compared to the dark condition, while the concentration of other positive ions is not changed. The corresponding chemical maps of these ions is shown in Figure S16. The pronounced decrease in concentration of $DFPD^+$ ion under illumination is possibly responsible for weakening or vanishing ferroelectricity observed in cKPFM measurements. This is because organic cations play an important role in determining ferroelectricity in 2D MHPs. When returning to dark condition, additional decreases in the concentration of other positive ions (MA^+ and other organic products) as well as the $DFPD^+$ ion are observed. An unknown organic component is detected at mass between 80 and 100, marked with a star in Figure 5a, which possibly originates from decomposition of organic component under illumination. Recently, we observed organic component decomposition using time-resolved ToF-SIMs in $MAPbI_3$ thin film in a lateral electrode device which is attributed to the bias-induced decomposition of MA^+ organic cation.[58] In this study[58], the mass spectra of positive ions showed several peaks that are associated with the byproducts of MA^+ decomposition appearing at masses between 40 and 80. Thus, the unknow organic component could be responsible for decomposition of $DFPD^+$

cation. This result indicates that the change in the organic cation chemistry can result in weakening of ferroelectricity and the loss of dipole moment.

As can be seen in the mass spectra of negative ions (Figure 5b), we observe relatively stable I^- ion dynamics in dark and under illumination, while the concentration of F^- ion decreases significantly under illumination and this change is not recoverable. The corresponding chemical maps are displayed in Figure S17. We speculate that this phenomenon results from decomposition of DFPD component (containing F^- ions) as observed in positive ion dynamics. Interestingly, we observe a depleted region in larger scan areas (100 μm^2) in the F^- ion map after the above ToF-SIMS measurements (see Figure S18). These results further confirm unstable chemical dynamics in $(4,4\text{-DFPD})_2PbI_4$ perovskites under illumination which leads to light-induced ferroelectricity modulation.

Compared to 3D (ABX_3) MHPs, there is a wide variety of candidates for the A-site cation in 2D (A_2BX_4) MHPs with longer organic chains, leading to enhanced stability under ambient conditions due to the hydrophobicity of the long chain cations. However, considering the molecular structure, structural difference, and their polarization, different ferroelectricity behavior in distinct MHPs structure and composition can be speculated. For instance, the size of A-site cation in 3D MHPs is limited to around 2.6 Å by Goldschmidt geometry rules[59]. In comparison, for 2D MHPs, not only the size of the cation is relatively larger but also the separated layer (quantum wells) thickness by the cation is larger over 10 Å. The unique larger A-site cation and structure in 2D MHPs provide additional asymmetry, which results in ferroelectricity classified as the order-disorder type. While 3D MHPs show relatively lower ferroelectric responses that originate from displacement of smaller A-site cation called displacive type. The difference of these molecular structures thus leads to different rotational properties of the polar cations in 3D and 2D MHPs. Therefore, significantly different ferroelectric dynamics can be expected in two different class of MHPs.

As discussed, in 2D MHPs, the organic cation motions are responsible for ferroelectricity. Particularly, multiple quantum wells where organic cations are placed between inorganic layers leads to higher ferroelectricity in 2D MHPs. In our study, the observed phenomenon can be dependent on the stability of organic cations under illumination and biasing conditions. Here, tunning preferential crystallographic directions can result in vanishing the ferroelectricity. In fact, spontaneous polarization which is an indication of ferroelectricity is very different in variety of organic cations as well as halide ions.[9]

We have explored ferroelectricity and the origin of light-ferroelectricity interaction using BE-PFM, cKPFM, in-situ XRD, and ToF-SIMS measurements. In the dark, ferroelectricity is confirmed by hysteretic behaviors in cKPFM responses. Under illumination, the observed ferroelectricity experiences a transition to the paraelectric phase. In MHPs, organic molecule cations play a critical role in determining the polarization where their orientation causes local potential fluctuations leading to highly orientated ferroelectric domain structures and domain walls.[60-62] These localized features improve charge carrier transport by reducing carrier recombination[63] as the existence of ferroelectric domains prevent from scattering of charge carriers[64]. Although a light-driven giant dielectric constant was observed in 3D MHPs[33, 65], weakening ferroelectricity under illumination is a unique characteristic in 2D MHPs. Previously, light-induced polarization reordering has been proposed as the origin of the improved ferroelectricity under illumination in 3D MHPs.[66, 67] This phenomenon was explained by reordering of the organic cation dipole moments under illumination resulting from variation in crystallographic orientation.[68] For example, [110] direction that is composed of head-to-head and tail-to-tail components where head-to-head component presents the same polarization direction and tail-to-tail component represents the opposite polarization direction leads to stronger one-dimensional potential wells, thus creating higher ferroelectricity.[68] On the contrary, 2D MHP contains layer-by-layer potential wells where perpendicular direction [001] to the layer is associated with ferroelectricity. This structural characteristic has led to higher ferroelectricity in 2D MHPs rather than in 3D MHP.[9] However, based on our results, light-driven preferential orientation modulation, e.g. decreased intensity of (1 1 1) lattice planes can lead to weakening of ferroelectricity, possibly resulting from minor structural variations. Further, the instability of organic cation due to ion migration or volatility under illumination could result in degradation and result in disappearance of ferroelectricity. Note that the ion migration under illumination can also screen ferroelectric polarization[46]. This study elucidates the origin of ferroelectric instability in $(4,4\text{-DFPD})_2PbI_4$ thin films which is important for clarifying light-ferroelectric interaction in 2D MHPs.

Conclusions

In summary, the BE-PFM measurements demonstrate ferroelectric domain structures on the $(4,4\text{-DFPD})_2PbI_4$ 2D film surface in dark and under illumination. The c-KPFM responses reveal hysteretic cKPFM loops in dark. The hysteretic dynamics are highly

dependent on domain structures in dark. However, hysteresis is dramatically reduced in the same region under illumination. The XRD results under illumination provide information of crystallographic orientation change. Specifically, the intensities on both (0 2 0) and (1 1 1) lattice planes are decreased under illumination. The reduction in the intensity of (1 1 1) plane that is associated with ferroelectric phase in this material can contribute to the transition from ferroelectricity to paraelectricity under illumination. Further, the chemical analysis using ToF-SIMS reveals that the positive organic cation and the corresponding negative F^- ion are unstable under illumination while concentration of I^- negative ion remains constant during the measurements. Consequently, both crystallinity and chemical dynamics can influence on ferroelectric properties in $(4,4\text{-DFPD})_2PbI_4$ thin films. These results highlight that the light-ferroelectricity interaction originates from crystallographic orientations and chemical composition instability in 2D MHPs. We highlight that the crystallographic and chemical engineering is the key element for more stable ferroelectricity in 2D MHPs.

Acknowledgments

M.A. acknowledges support from National Science Foundation (NSF), Award Number # 2043205. D.K. and M.A. acknowledge support from the University of Tennessee and CNMS user facility, project # CNMS**2021-A-00706**. The ToF-SIMS measurements were conducted and supported (A. V. I, S. V. K.) at the Center for Nanophase Materials Science (CNMS), which is a DOE Office of Science User Facility. S.V.K. acknowledges the support of the 3DFeM EFRC center. XRD was performed at the Institute for Advanced Materials and Manufacturing (IAMM) Diffraction Facility, located at the University of Tennessee, Knoxville.

CrediT authorship contribution statement

Dohyung Kim: Conceptualization, Investigation, Validation, Resources, Data Curation, Visualization, Writing – original draft. **Anton V. Ievlev**: Investigation, Data curation, Visualization, Writing – review & draft. **Olga S. Ovchinnikova**: Resources, Writing – review & draft. **Sergei V. Kalinin**: Conceptualization, Writing – review & draft. **Mahshid Ahmadi**: Conceptualization, Supervision, Project administration, Funding acquisition, Writing – review & draft.

Conflict of Interest

The authors declare no conflict of interest.

Experimental Section

Single crystal growth: (4,4-difluoropiperidinium)$_2$PbI$_4$ single crystals were grown by slow cooling crystallization. 4,4-difluoropiperidinium hydrochloride (DFPD, 0.1M, Sigma-Aldrich) are dissolved in the HI solution (10 mL, 57wt% in H_2O, Sigma-Aldrich), and then stirred at room temperature for 1hr. Then PbI_2 (0.05M, Sigma-Aldrich) is added to the solution. An orange powder precipitates from the undissolved PbI_2 which was dissolved by heating the solution to 405 K in an oil bath. The solution was kept at the same temperature for 1 h, forming a clear solution. Slowly cooling the solution to room temperature for around 14 days produced needle shape crystals of (4,4-DFPD)$_2$PbI$_4$.

Thin film fabrications: The as-grown (4,4-DFPD)$_2$PbI$_4$ crystals (60 mg) are dissolved in dimethyl sulfoxide (DMSO, 200 μL) to prepare the precursor solution. The ITO (Indium tin

oxide)-coated glass substrates (MSE Pro^{TM}, 15×15×1 mm^3) were precleaned using deionized water, acetone, and isopropanol in an ultrasonic bath for 15 mins, respectively. After the initial cleaning, the glass substrates were treated under UV ozone for 15 mins. Then, the substrates were transferred into an N_2-filled glove box. For drop-casting, a precleaned ITO glass was placed on a hotplate at 373K, and then about 5 μL of precursor solution was carefully dropped on the hot substrate and dried for 10 min for full crystallization.

Characterizations and data analysis

Scanning probe microscopy (SPM) measurements: AFM, PFM, BE-PFM, cKPFM

The thin films were characterized by atomic force microscopy (AFM, MFP-3D, Asylum Research) under the ambient condition at room temperature. All SPM measurements were performed using a Pt/Ir coated Si cantilever (ElectriMulti 75-G, Budget Sensors). For piezo-response force microscopy (PFM), AC drive amplitude (3V) was applied to the PFM tip to achieve a sharp contact resonance peak. All PFM data were obtained with out-of-plane amplitude and phase in the same scan. For illumination, white LED sources that are not filtered illuminate the sample from the bottom area through the glass substrate. In all PFM measurements, the scan rate is fixed at 1.0 Hz, and the scan direction starts from the top to bottom.

Band-excitation piezo-response force microscopy (BE-PFM) and contact Kelvin probe force microscopy (cKPFM) measurements: Band excitation (BE)-PFM and contact Kelvin probe force microscopy (cKPFM) were carried out using an AFM (MFP-3D, Asylum Research) with in-house controller (Look Instrument) and Labview-based software. The same AFM tip was used as above. BE mode uses a digitally synthesized AC voltage across a range of frequencies. A built-in lock-in amplifier was used to enhance the signal to noise in all BE-PFM and cKPFM measurements. The frequency range in the BE measurements was centered at 380 kHz with a bandwidth of 100 kHz, and the drive amplitude for BE-PFM excitation was 3 V. The BE-PFM measurements were taken over a grid of 256 ×256 points on the sample surface. BE-PFM responses such as amplitude, phase, frequency, and Q-factor are obtained using a simple harmonic oscillator (SHO) model. The cKPFM measurements were taken over a grid of 40 by 40 points on the film surface. For the cKPFM measurements, a DC write voltage was applied stepwise from 0, +10 V, 0 V, -10V, and back to zero consecutively with totally 32 steps. These applied voltage steps are referred to as V_{write}. Between all V_{write} steps, there is a read bias step

(V_{read}), where the piezo-response and cKPFM response are measured with totally 7 steps between -10 to +10 V. The delay time between subsequent measurements is in the milliseconds. The piezo-response measured at 0 V during the read measurements is shown in the off-field response. Likewise, the sample was illuminated from the white LED source sources located at the bottom area.

Principle component analysis (PCA) in cKPFM data: the 4D cKPFM data set can be well represented as a bimodal 3D data set $R_{av}(V_{read}, x, y)$ and $R_{delta}(V_{read}, x, y)$. R_{av} represents the average V_{read} and R_{delta} represents the corresponding dispersion. PCA is performed using pycroscopy based on universal spectroscopy and imaging data model on Jupyter Notebook for Python 3. To gain PCA components and the corresponding loading maps from the mean deviation of the cKPFM data, these are computed using Scikit-Learn's PCA estimator.

X-ray diffraction (XRD) measurements: The crystal structure and crystal orientation of the films were characterized by a high-resolution X-ray diffractometer (X'Pert Pro, Panalytical). The X-ray diffractometer uses Cu Kα radiation.

Time-of-flight-secondary ion mass spectrometry (ToF-SIMS) measurements: ToF-SIMS measurements were performed using ToF.SIMS-5-NCS instrument (IONTOF GmbH, Germany). Experiments were carried out in both negative and positive ion modes with spectra calibrated using the I^-, F^-, $C_5H_9F_2N^+$ and Pb^+ peaks. A built-in LED white light in the ToF-SIMS chamber is used for illumination.

First-order reversal curve (FORC) biases with on- and off-field on the planar electrode device: The FORC waveform electrical biases with on- and off-field were applied to the planar electrode devices. The electrical biases were supplied by a Keithley 2450 source meter controlled by a test script builder. The current was collected simultaneously by the source meter. A commercial white LED source was used for illumination.

References

1. W. Li, Z. Wang, F. Deschler, S. Gao, R. H. Friend and A. K. Cheetham, *Nature Reviews Materials*, 2017, **2**, 16099.
2. G. Long, R. Sabatini, M. I. Saidaminov, G. Lakhwani, A. Rasmita, X. Liu, E. H. Sargent and W. Gao, *Nature Reviews Materials*, 2020, **5**, 423-439.
3. Y. Fu, H. Zhu, J. Chen, M. P. Hautzinger, X. Y. Zhu and S. Jin, *Nature Reviews Materials*, 2019, **4**, 169-188.
4. G. Grancini and M. K. Nazeeruddin, *Nature Reviews Materials*, 2019, **4**, 4-22.
5. I. C. Smith, E. T. Hoke, D. Solis-Ibarra, M. D. McGehee and H. I. Karunadasa, *Angewandte Chemie International Edition*, 2014, **53**, 11232-11235.
6. F. O. Saouma, C. C. Stoumpos, J. Wong, M. G. Kanatzidis and J. I. Jang, *Nature Communications*, 2017, **8**, 742.
7. R. Zhuang, X. Wang, W. Ma, Y. Wu, X. Chen, L. Tang, H. Zhu, J. Liu, L. Wu, W. Zhou, X. Liu and Y. Yang, *Nature Photonics*, 2019, **13**, 602-608.
8. M. Seitz, A. J. Magdaleno, N. Alcázar-Cano, M. Meléndez, T. J. Lubbers, S. W. Walraven, S. Pakdel, E. Prada, R. Delgado-Buscalioni and F. Prins, *Nature Communications*, 2020, **11**, 2035.
9. Y. Hou, C. Wu, D. Yang, T. Ye, V. G. Honavar, A. C. T. van Duin, K. Wang and S. Priya, *Journal of Applied Physics*, 2020, **128**, 060906.
10. J. F. Scott, *Science*, 2007, **315**, 954.
11. W.-Q. Liao, Y. Zhang, C.-L. Hu, J.-G. Mao, H.-Y. Ye, P.-F. Li, S. D. Huang and R.-G. Xiong, *Nature Communications*, 2015, **6**, 7338.
12. H.-Y. Ye, W.-Q. Liao, C.-L. Hu, Y. Zhang, Y.-M. You, J.-G. Mao, P.-F. Li and R.-G. Xiong, *Advanced Materials*, 2016, **28**, 2579-2586.
13. C. Ji, S. Wang, L. Li, Z. Sun, M. Hong and J. Luo, *Advanced Functional Materials*, 2019, **29**, 1805038.
14. C.-K. Yang, W.-N. Chen, Y.-T. Ding, J. Wang, Y. Rao, W.-Q. Liao, Y.-Y. Tang, P.-F. Li, Z.-X. Wang and R.-G. Xiong, *Advanced Materials*, 2019, **31**, 1808088.
15. P.-P. Shi, S.-Q. Lu, X.-J. Song, X.-G. Chen, W.-Q. Liao, P.-F. Li, Y.-Y. Tang and R.-G. Xiong, *Journal of the American Chemical Society*, 2019, **141**, 18334-18340.
16. H. Fu, C. Jiang, J. Lao, C. Luo, H. Lin, H. Peng and C.-G. Duan, *CrystEngComm*, 2020, **22**, 1436-1441.
17. H.-Y. Zhang, X.-J. Song, X.-G. Chen, Z.-X. Zhang, Y.-M. You, Y.-Y. Tang and R.-G. Xiong, *Journal of the American Chemical Society*, 2020, **142**, 4925-4931.
18. X.-G. Chen, X.-J. Song, Z.-X. Zhang, H.-Y. Zhang, Q. Pan, J. Yao, Y.-M. You and R.-G. Xiong, *Journal of the American Chemical Society*, 2020, **142**, 10212-10218.
19. X.-G. Chen, X.-J. Song, Z.-X. Zhang, P.-F. Li, J.-Z. Ge, Y.-Y. Tang, J.-X. Gao, W.-Y. Zhang, D.-W. Fu, Y.-M. You and R.-G. Xiong, *Journal of the American Chemical Society*, 2020, **142**, 1077-1082.
20. H.-Y. Liu, H.-Y. Zhang, X.-G. Chen and R.-G. Xiong, *Journal of the American Chemical Society*, 2020, **142**, 15205-15218.
21. H.-Y. Zhang, Y.-Y. Tang, P.-P. Shi and R.-G. Xiong, *Accounts of Chemical Research*, 2019, **52**, 1928-1938.
22. Y.-Y. Tang, Y. Xie, Y.-L. Zeng, J.-C. Liu, W.-H. He, X.-Q. Huang and R.-G. Xiong, *Advanced Materials*, 2020, **32**, 2003530.
23. Z.-X. Wang, Y. Zhang, Y.-Y. Tang, P.-F. Li and R.-G. Xiong, *Journal of the American Chemical Society*, 2019, **141**, 4372-4378.
24. D. Kim, B. Dryzhakov, Y. Liu, O. S. Ovchinnikova, B. Hu, S. V. Kalinin and M. Ahmadi, *Chemistry of Materials*, 2021, **33**, 4077-4088.
25. R. Pandey, G. Vats, J. Yun, C. R. Bowen, A. W. Y. Ho-Baillie, J. Seidel, K. T. Butler and S. I. Seok, *Advanced Materials*, 2019, **31**, 1807376.
26. A. N. Morozovska, E. A. Eliseev, N. V. Morozovsky and S. V. Kalinin, *Physical Review B*, 2017, **95**, 195413.

27. Y. Liu, D. Kim, A. V. Ievlev, S. V. Kalinin, M. Ahmadi and O. S. Ovchinnikova, *Advanced Functional Materials*, 2021, **n/a**, 2102793.
28. Y.-T. Li, L. Ding, J.-Z. Li, J. Kang, D.-H. Li, L. Ren, Z.-Y. Ju, M.-X. Sun, J.-Q. Ma, Y. Tian, G.-Y. Gou, D. Xie, H. Tian, Y. Yang, L.-W. Wang, L.-M. Peng and T.-L. Ren, *ACS Central Science*, 2019, **5**, 1857-1865.
29. S. Jariwala, H. Sun, G. W. P. Adhyaksa, A. Lof, L. A. Muscarella, B. Ehrler, E. C. Garnett and D. S. Ginger, *Joule*, 2019, **3**, 3048-3060.
30. S. Y. Leblebici, L. Leppert, Y. Li, S. E. Reyes-Lillo, S. Wickenburg, E. Wong, J. Lee, M. Melli, D. Ziegler, D. K. Angell, D. F. Ogletree, Paul D. Ashby, F. M. Toma, J. B. Neaton, I. D. Sharp and A. Weber-Bargioni, *Nature Energy*, 2016, **1**, 16093.
31. D. Kim, J.-H. Yun, M. Lyu, J. Kim, S. Lim, J. S. Yun, L. Wang and J. Seidel, *The Journal of Physical Chemistry C*, 2019, **123**, 14144-14151.
32. Y. Liu, P. Trimby, L. Collins, M. Ahmadi, A. Winkelmann, R. Proksch and O. S. Ovchinnikova, *ACS Nano*, 2021, **15**, 7139-7148.
33. E. J. Juarez-Perez, R. S. Sanchez, L. Badia, G. Garcia-Belmonte, Y. S. Kang, I. Mora-Sero and J. Bisquert, *The Journal of Physical Chemistry Letters*, 2014, **5**, 2390-2394.
34. M. Coll, A. Gomez, E. Mas-Marza, O. Almora, G. Garcia-Belmonte, M. Campoy-Quiles and J. Bisquert, *The Journal of Physical Chemistry Letters*, 2015, **6**, 1408-1413.
35. D. Kim, J. S. Yun, P. Sharma, D. S. Lee, J. Kim, A. M. Soufiani, S. Huang, M. A. Green, A. W. Y. Ho-Baillie and J. Seidel, *Nature Communications*, 2019, **10**, 444.
36. R. K. Vasudevan, N. Balke, P. Maksymovych, S. Jesse and S. V. Kalinin, *Applied Physics Reviews*, 2017, **4**, 021302.
37. N. Balke, P. Maksymovych, S. Jesse, A. Herklotz, A. Tselev, C.-B. Eom, I. I. Kravchenko, P. Yu and S. V. Kalinin, *ACS Nano*, 2015, **9**, 6484-6492.
38. Y. Liu, N. Borodinov, M. Lorenz, M. Ahmadi, S. V. Kalinin, A. V. Ievlev and O. S. Ovchinnikova, *Advanced Science*, 2020, **7**, 2001176.
39. M. Ahmadi, L. Collins, K. Higgins, D. Kim, E. Lukosi and S. V. Kalinin, *ACS Applied Materials & Interfaces*, 2019, **11**, 41551-41560.
40. D. Kim, E. S. Muckley, N. Creange, T. H. Wan, M. H. Ann, E. Quattrocchi, R. K. Vasudevan, J. H. Kim, F. Ciucci, I. N. Ivanov, S. V. Kalinin and M. Ahmadi, *Advanced Science*, 2021, **8**, 2002510.
41. D. Kim, Y. Liu, A. V. Ievlev, K. Higgins, O. S. Ovchinnikova, J. S. Yun, J. Seidel, S. V. Kalinin and M. Ahmadi, *Nano Energy*, 2021, **89**, 106428.
42. J. S. Yun, J. Seidel, J. Kim, A. M. Soufiani, S. Huang, J. Lau, N. J. Jeon, S. I. Seok, M. A. Green and A. Ho-Baillie, *Advanced Energy Materials*, 2016, **6**, 1600330.
43. M. H. Futscher, J. M. Lee, L. McGovern, L. A. Muscarella, T. Wang, M. I. Haider, A. Fakharuddin, L. Schmidt-Mende and B. Ehrler, *Materials Horizons*, 2019, **6**, 1497-1503.
44. Y. Lin, Y. Bai, Y. Fang, Q. Wang, Y. Deng and J. Huang, *ACS Energy Letters*, 2017, **2**, 1571-1572.
45. D. Kim, R. K. Vasudevan, K. Higgins, A. Morozovska, E. A. Eliseev, M. Ziatdinov, S. V. Kalinin and M. Ahmadi, *The Journal of Physical Chemistry C*, 2021, **125**, 12355-12365.
46. M. Ahmadi, L. Collins, A. Puretzky, J. Zhang, J. K. Keum, W. Lu, I. Ivanov, S. V. Kalinin and B. Hu, *Advanced Materials*, 2018, **30**, 1705298.
47. A. Gruverman, M. Alexe and D. Meier, *Nature Communications*, 2019, **10**, 1661.
48. N. Balke, P. Maksymovych, S. Jesse, I. I. Kravchenko, Q. Li and S. V. Kalinin, *ACS Nano*, 2014, **8**, 10229-10236.
49. D. Kim, R. K. Vasudevan, K. Higgins, A. Morozovska, E. A. Eliseev, M. Ziatdinov, S. V. Kalinin and M. Ahmadi, *The Journal of Physical Chemistry C*, 2021, **125**, 12355-12365.
50. S. M. Yang, A. N. Morozovska, R. Kumar, E. A. Eliseev, Y. Cao, L. Mazet, N. Balke, S. Jesse, R. K. Vasudevan, C. Dubourdieu and S. V. Kalinin, *Nature Physics*, 2017, **13**, 812-818.
51. S. V. Kalinin, A. N. Morozovska, L. Q. Chen and B. J. Rodriguez, *Reports on Progress in Physics*, 2010, **73**, 056502.
52. H. Borkar, V. Rao, M. Tomar, V. Gupta, J. F. Scott and A. Kumar, *Materials Today Communications*, 2018, **14**, 116-123.

53. H. Borkar and A. Kumar, *Vacuum*, 2018, **153**, 91-95.
54. Y. Yuan, Q. Wang, Y. Shao, H. Lu, T. Li, A. Gruverman and J. Huang, *Advanced Energy Materials*, 2016, **6**, 1501803.
55. N.-K. Kim, S.-J. Yeom, S.-Y. Kweon, E.-S. Choi, H.-J. Sun, H.-C. Sohn and J.-S. Roh, *Integrated Ferroelectrics*, 2005, **70**, 89-97.
56. R. Ding, D. Wang, D. Chu and S. Li, *Journal of the American Ceramic Society*, 2013, **96**, 3530-3535.
57. R. Ramesh, T. Sands and V. G. Keramidas, *Applied Physics Letters*, 1993, **63**, 731-733.
58. Y. Liu, N. Borodinov, L. Collins, M. Ahmadi, S. V. Kalinin, O. S. Ovchinnikova and A. V. Ievlev, *ACS Nano*, 2021, DOI: 10.1021/acsnano.1c02097.
59. J.-P. Correa-Baena, M. Saliba, T. Buonassisi, M. Grätzel, A. Abate, W. Tress and A. Hagfeldt, *Science*, 2017, **358**, 739-744.
60. J. M. Frost, K. T. Butler, F. Brivio, C. H. Hendon, M. van Schilfgaarde and A. Walsh, *Nano Letters*, 2014, **14**, 2584-2590.
61. J. M. Frost, K. T. Butler and A. Walsh, *APL Materials*, 2014, **2**, 081506.
62. S. Liu, F. Zheng, N. Z. Koocher, H. Takenaka, F. Wang and A. M. Rappe, *The Journal of Physical Chemistry Letters*, 2015, **6**, 693-699.
63. A. Pecchia, D. Gentilini, D. Rossi, M. Auf der Maur and A. Di Carlo, *Nano Letters*, 2016, **16**, 988-992.
64. K. Miyata and X. Y. Zhu, *Nature Materials*, 2018, **17**, 379-381.
65. I. Anusca, S. Balčiūnas, P. Gemeiner, Š. Svirskas, M. Sanlialp, G. Lackner, C. Fettkenhauer, J. Belovickis, V. Samulionis, M. Ivanov, B. Dkhil, J. Banys, V. V. Shvartsman and D. C. Lupascu, *Advanced Energy Materials*, 2017, **7**, 1700600.
66. T. Wu, L. Collins, J. Zhang, P.-Y. Lin, M. Ahmadi, S. Jesse and B. Hu, *ACS Nano*, 2017, **11**, 11542-11549.
67. P. Wang, J. Zhao, L. Wei, Q. Zhu, S. Xie, J. Liu, X. Meng and J. Li, *Nanoscale*, 2017, **9**, 3806-3817.
68. H.-C. Hsu, B.-C. Huang, S.-C. Chin, C.-R. Hsing, D.-L. Nguyen, M. Schnedler, R. Sankar, R. E. Dunin-Borkowski, C.-M. Wei, C.-W. Chen, P. Ebert and Y.-P. Chiu, *ACS Nano*, 2019, **13**, 4402-4409.